Supporting Information

Fluorine-Doped 3D Honeycomb Carbon Network for Long-Duration Aqueous Zinc-Iodine Batteries

Wenwen Cao[1, 2#], Zhenglin Li[1,3#], Haichao Huang[4*], Tao Hu[4], Yuanwei Zhang[5], Chenxi Dong[1], Haibo Hu[4], Yiqiang Sun[2*], Guojin Liang[1*]

[1]Faculty of Materials Science and Energy Engineering, Shenzhen University of Advanced Technology, Shenzhen 518055, China.
[2]School of Chemistry and Chemical Engineering, University of Jinan, Jinan, 250055, P. R. China.
[3]School of Chemistry and Chemical Engineering, State Key Laboratory of Synergistic Chem-Bio Synthesis, Frontiers Science Center for Transformative Molecules, State Key Laboratory of Micro-Nano Engineering Science, Shanghai Jiao Tong University, Shanghai 200240, China.
[4]School of Materials Science and Engineering, Anhui University, Hefei 230601, China.
[5]Institute of Technology for Carbon Neutrality, Shenzhen Institutes of Advanced Technology, Chinese Academy of Sciences, Shenzhen 518055, China.
#These authors contributed equally.
*Email: huanghc1@foxmail.com; haibohu@ahu.edu.cn; chm_sunyq@ujn.edu.cn; gj.liang@siat.ac.cn

1. Experimental section

1.1 Materials

All chemicals were used without further purification. Sodium carboxymethyl cellulose (CMC, analytical grade), sodium bicarbonate ($NaHCO_3$, ≥99%), ammonium fluoride (NH_4F, ≥98%), iodine (I_2, ≥99%), poly(vinylidene fluoride) (PVDF, ≥99.5%, Mw≈71,000), N-methyl-2-pyrrolidone (NMP, ≥99%), zinc iodide (ZnI_2, ≥99%), potassium iodide (KI, chemically pure), zinc sulfate heptahydrate ($ZnSO_4·7H_2O$, ≥99%), and hydrochloric acid (HCl, 37 wt%) were obtained from Aladdin Biochemical Technology Co., Ltd. (Shanghai, China). Ultrapure water (resistivity: 18.25 MΩ·cm) was provided by Ecolab Inc. (USA). Anhydrous ethanol (≥99%) was purchased from Sinopharm Chemical Reagent Co., Ltd. (China). Zinc foil (0.01 mm, 99.9%), titanium foil (0.01 mm, 99.9%), and stainless steel mesh (100 mesh) all were obtained from Shengshida Metal Materials Co., Ltd. (Dongguan, China). Ketjen black (EC-600JD) was purchased from Lion Corporation (Japan). High-purity nitrogen gas (N_2, ≥99.999%).

1.2 Synthesis of 3D Honeycomb-Like Carbon Nano-Network (Cnet) and Fluorine-Doped Cnet (F-Cnet)

Initially, 100 mg of carboxymethyl cellulose (CMC) and 100, 200, 300, and 400 mg of sodium bicarbonate ($NaHCO_3$) were mixed at different mass ratios (1:1, 1:2, 1:3, and 1:4) by thorough grinding in a mortar to ensure uniform blending. The resulting mixture was transferred into a ceramic boat and heated under a nitrogen (N_2) atmosphere at a ramping rate of 5 °C min^{-1} to 800 °C, where it was maintained for 2 h before naturally cooling to room temperature. The resulting black product was repeatedly washed with deionized (DI) water and dilute hydrochloric acid (HCl) until the pH of the supernatant reached 7. After centrifugation to remove residual impurities, the collected solid was dried under vacuum at 60 °C for 12 h to obtain the 3D honeycomb-like carbon nano-network precursor, denoted as Cnet. For fluorine doping, 100 mg of the dried Cnet powder was evenly ground and transferred into a ceramic boat. To prepare the fluorine precursor, ammonium fluoride (NH_4F) was used in various mass ratios relative to Cnet: 1:1, 1:3, 1:5, 1:7, and 1:10. The optimal mass ratio was found to be 1:5, where 100 mg of Cnet was mixed with 500 mg of NH_4F. The precursor was placed in a ceramic boat located upstream in the gas flow direction of a tubular furnace, while the boat containing Cnet was placed downstream. The system was purged with nitrogen gas (flow rate: 2 mL s^{-1}), and the furnace was heated to 400 °C at a rate of 10 °C min^{-1} and held for 1 h before naturally cooling to room temperature. The resulting product was denoted as F-Cnet, a 3D fluorine-doped honeycomb-like carbon nano-network.

1.3 Fabrication of I_2@F-Cnet Composite Electrodes

To fabricate the composite electrode, F-Cnet, Ketjen Black, and polyvinylidene fluoride (PVDF) were mixed in a weight ratio of 8:1:1 and dispersed in N-methyl-2-pyrrolidone (NMP). The slurry was stirred continuously for 12 h to ensure homogeneity and then uniformly coated onto stainless steel foil. The coated foil was dried in a vacuum oven at 60 °C for 12 h. After drying, electrode sheets with an area of 1×1 cm^2 were cut and subjected to galvanostatic electrodeposition (5 mA, 12 min) to load iodine, yielding an iodine loading of 4.7 mg cm^{-2}. For higher iodine loadings, the electrodeposition duration was extended to 36 mins and 60 mins, achieving iodine loadings of

14.1 mg cm^{-2} and 23.5 mg cm^{-2}, respectively. The electrodeposition was conducted in a two-electrode glass cell using a mixed electrolyte of 0.5 M ZnI_2 and 0.5 M KI. Both I_2@F-Cnet and I_2@Cnet electrodes with different iodine contents were prepared in this way. After deposition, the electrodes were rinsed with DI water and dried in a vacuum oven at 30 °C. During cell assembly, the I_2@F-Cnet (or I_2@Cnet) electrode served as the cathode, zinc foil was used as the anode (N/P ratio = 2.0), and 2 M $ZnSO_4$ was used as the electrolyte (E/C ratio = 11.3 g Ah^{-1}). A water glass membrane with a thickness of 100 μm served as the separator. All I_2@F-Cnet electrodes in this work are prepared by a conventional slurry-casting process in which the F-Cnet host, conductive additive and binder are dispersed into a slurry and doctor-bladed as a single-side coating onto a commercial current collector, followed by standard drying and electrode cutting. This fabrication route is fully compatible with roll-to-roll electrode production. To further demonstrate scalability and compatibility with practical cell configurations, we assembled a pouch cell using a slurry-cast I_2@F-Cnet cathode, commercial Zn foil as the anode, a glass-fiber separator, Al-plastic laminate packaging and Ni/Al tabs.

1.4 Electrochemical Characterizations

The electrochemical testing of batteries was performed using a CHI 760E electrochemical workstation and Land 2001A battery test system. The cathode scan started at the voltage of the open circuit potential. The electrochemical impedance spectrum (EIS) was obtained by applying a perturbation signal of 5 mV s^{-1} with alternating current in a frequency range from 0.1 Hz to 100 kHz during the CV scan. DRT was a model-free approach that avoided pre-modeling of the electrochemical system and could reveal clear time-domain signatures. Conventional electrochemical analysis of EIS in battery systems relied on empirically based models, which often missed new electrochemical details. EIS, as one of the most important electrochemical methods, obtained rich internal information when combined with in situ galvanostatic electrochemical impedance spectroscopy. Accurate interpretation of EIS was critical. The DRT transformation, optimized by the Tikhonov regularization method, offered a promising solution for further analyzing EIS.

2. Material Characterizations

XRD measurements were carried out on a Bruker D8-Advance powder X-ray diffractometer operating at 40 kV and 30 mA, using Cu-Kα radiation (λ = 0.15405 nm). Transmission electron microscope (TEM, JEOL, JEM-2100F, 200 kV) and high-resolution TEM (HRTEM) were used to characterize the microstructure of the samples. The microstructure of the host was observed by a Field Emission Scanning Electron Microscope (FE-SEM, Regulus-8100, Japan). X-ray photoelectron spectroscopy (XPS) measurements were performed by a PHI Model 5802 spectrophotometer. Raman spectra were collected using a PerkinElmer Raman 400F spectrometer equipped with a 532 nm NIR laser. Brunauer-Emmett-Teller (BET) measurements were carried out on a JW-BK200C surface area analyzer operating at nitrogen atmosphere and the adsorption temperature of 77 k. Additionally, the UV-vis spectra of the $ZnSO_4$ electrolytes soaking different cathodes were collected to monitor the dissolution of the iodine species. Ion chromatography (IC) measurements were carried out on an ICS-1600 ion chromatograph (Dionex) using deionized water–based eluents under standard anion analysis conditions.

3. Theoretical Calculations of Optimal Battery Design Model for AZIBs

For the energy density and specific capacity at the electrode level in Figure 1, the functional relationship between the (gravimetric) energy density (E_G) of the full cell and the cathode loading (x) is as follows:

$$E_G = \frac{V \times SC_{cell}}{(E/C) * x + \frac{N/P}{0.82} * x + \frac{x}{SC_{cathode}} + m_{other}}$$

where the V represents the plateau voltage of the full cell, SC_{cell} is the theoretical specific capacity of the full cell, the E/C ratio is the ratio of the electrolyte weight to the cell capacity, the N/P ratio is the negative/positive capacity ratio, $SC_{cathode}$ is the theoretical specific capacity of the active materials of the cathode, mother refers to the masses of the separator, binder, conductive agent, and current collector.

Some researchers have already statistically provided parameters that are more in line with experimental realities: the N/P ratio is 1.1, the E/C ratio is 2.5 g Ah^{-1}, and the separator thickness is approximately 22 μm.[1-4] The theoretical capacity and energy density of iodine are 211 mAh g^{-1} and 274 Wh kg^{-1}, respectively, while the theoretical capacity of Zn is 820 mAh g^{-1}. Thus, the mass of the full battery could be computed as the formula:

$$m(kg) = (11.8x + 16.0) \times 10^{-6}$$

By substituting these determined parameters into the above formula, the curves between the energy density and the cathode capacity of different types of zinc-based batteries (Zn/I_2@Host, Zn/MnO_2, and $Zn/LiMn_2O_4$ cells) can be obtained.[5] Therefore, the energy density of the full battery could be calculated according to the equation:

$$E = \frac{1287.8x}{11.8x + 16.0}$$

4. Quantitative Analysis of Electrode Kinetics in CV

In CV tests, the relationship between peak current (i_p) and scan rate (v) is analyzed to determine the reaction control mechanism of the electrode. This relationship can be expressed using the following equation:

$$i_p = av^b$$

where i_p is the peak current (A), v is the scan rate (V s^{-1}), a is a constant, and b is the exponent that reflects the control mechanism of the electrode reaction. Specifically, the value of b can be interpreted as follows:

b=0.5: The reaction is diffusion-controlled.

b=1: The reaction is surface-controlled.

0.5<b<1: The reaction is a combination of diffusion and surface control.

By fitting the relationship between log i_p and log v, the value of b can be determined, thereby revealing the nature of the control mechanism. For diffusion-controlled reactions, the peak current is proportional to the square root of the scan rate ($v^{1/2}$):

$$i_p = kv^{1/2}$$

where k is a proportional constant, including factors such as the number of electrons involved, electrode area, diffusion coefficient, and reactant concentration. If i_p shows a linear relationship with $v^{1/2}$, this indicates that the reaction is diffusion-controlled.

5. Tafel Slope Calculation for Different Electrode Materials

Linear Sweep Voltammetry (LSV) is used to derive the Tafel equation, which provides insights into the kinetic parameters of electrode reactions, such as exchange current density (j_0) and Tafel slope (b). The Tafel equation describes the relationship between the current density (j) and overpotential (η):

$$\eta = a + b\log j$$

where η is the overpotential (V), a is the intercept of the Tafel equation, which is related to the exchange current density (j_0), b is the Tafel slope, which reflects the kinetics of the electrode reaction, j is the current density (A cm^{-2}).

The Tafel slope (b) provides valuable information on the reaction kinetics, with a smaller slope typically indicating a more efficient electrocatalytic process. Both CV and LSV tests are essential for evaluating and comparing the electrochemical behavior and performance of different electrode materials, providing quantitative insights into their reaction kinetics and control mechanisms.

6. Computational Methodology

First-principles calculations based on density functional theory (DFT) were performed using the Vienna Ab initio Simulation Package (VASP).[6] The electron exchange-correlation interactions were treated within the generalized gradient approximation (GGA) employing the Perdew-Burke-Ernzerhof (PBE) functional.[7] A plane-wave basis set with a kinetic energy cutoff of 400 eV was adopted to ensure the convergence of the total energy. The Brillouin zone was sampled using a Gamma-centered k-point mesh of size 1×1×1, chosen to balance computational cost with numerical accuracy. The electronic self-consistent iteration was considered converged when the energy difference between successive steps fell below 10^{-5} eV. Geometry optimization was carried out until the Hellmann-Feynman forces on all atoms were less than 0.01 eV/Å. To mitigate spurious interactions between periodic images, a vacuum layer of 20 Å was introduced along the z-direction in surface models. The Gibbs free energy change (ΔG) under standard conditions was computed using the thermodynamic expression:

$$\Delta G = \Delta E + \Delta ZPE - T\Delta S$$

Here, ΔE denotes the reaction energy difference derived from DFT total energies. ΔZPE is the change in zero-point energy.[8] The entropic contribution TΔS was determined from the vibrational density of states at 298.15 K, consistent with conventional treatments of entropy in solid-state systems.[9, 10]

7. Explanation of Practical Energy Density Calculations

The reported electrode energy density of 110.1 Wh kg^{-1} is calculated on the basis of the total cathode mass, including the active iodine, F-Cnet host, conductive additive, binder, and current collector. In our cell, the mass distribution is iodine (active species): 23.5 mg; F-Cnet host: 15.0 mg; conductive agent and binder: 2.4 mg; and current collector: 14.0 mg, giving a total cathode mass of 54.9 mg. Using the average discharge voltage of 1.21 V and the areal capacity of 5.0 mAh cm^{-2}, the specific energy based on the whole cathode is:

$$E_{total} = \frac{1.21\ V \times 5\ mAh}{0.0549\ g} \approx 110.1\ Wh\ kg^{-1}$$

For transparency and better comparison with the literature, we have also calculated the energy

density based solely on the mass of the active iodine:

$$E_{I2} = \frac{1.21\ V \times 5\ mAh}{0.0235\ g} \approx 257\ Wh\ kg^{-1}$$

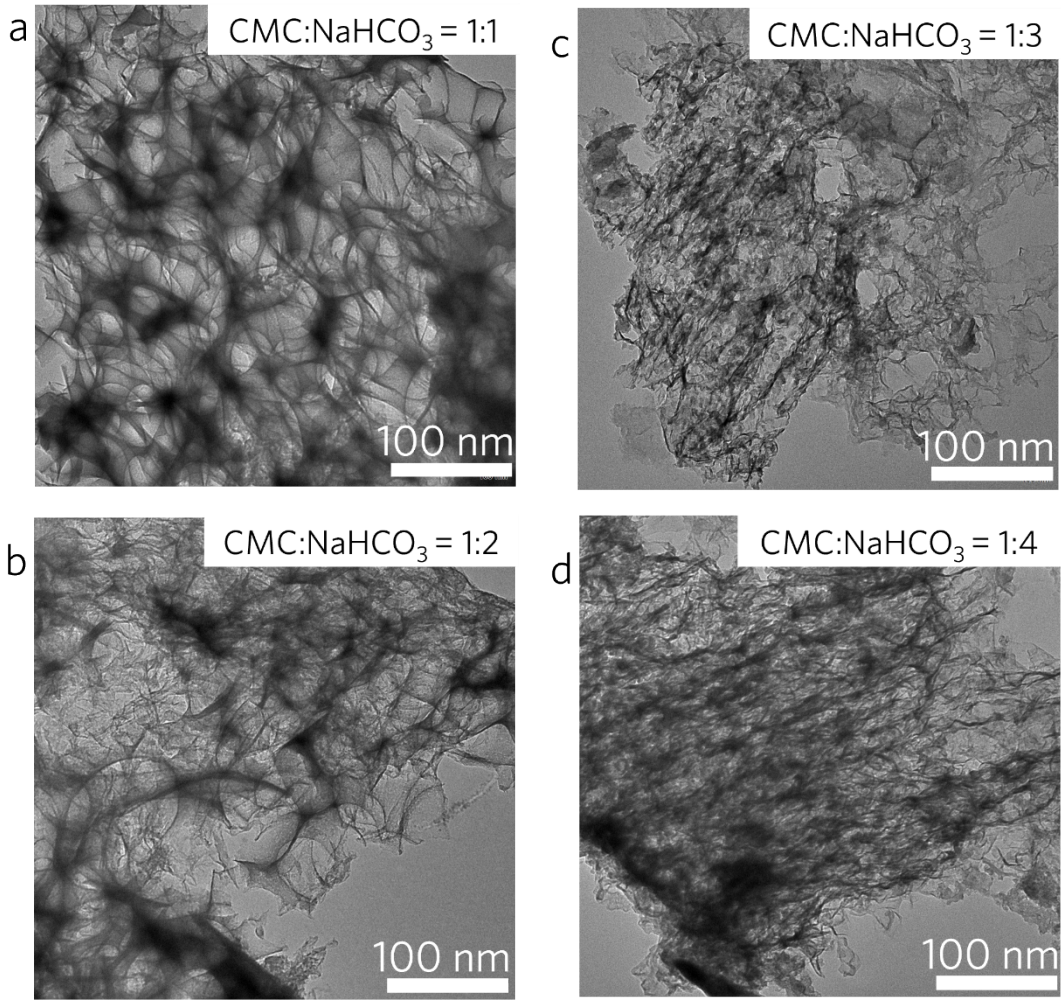

Figure S1. TEM images of Cnet prepared at different CMC/$NaHCO_3$ mass ratios (1:1, 1:2, 1:3, 1:4), showing morphology evolution.

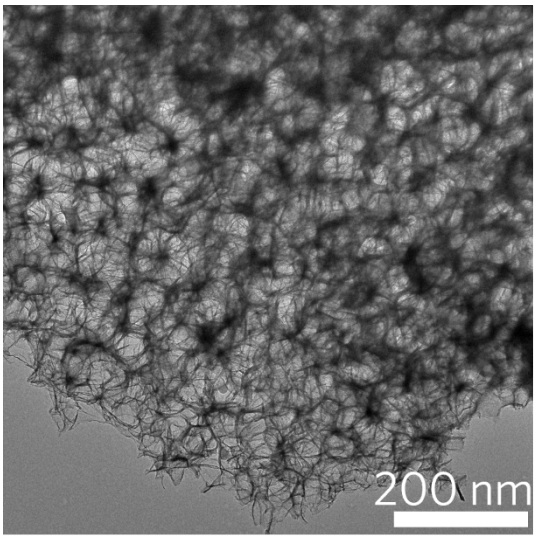

Figure S2. TEM image of Cnet obtained at the optimized CMC/$NaHCO_3$ mass ratio 1:1.

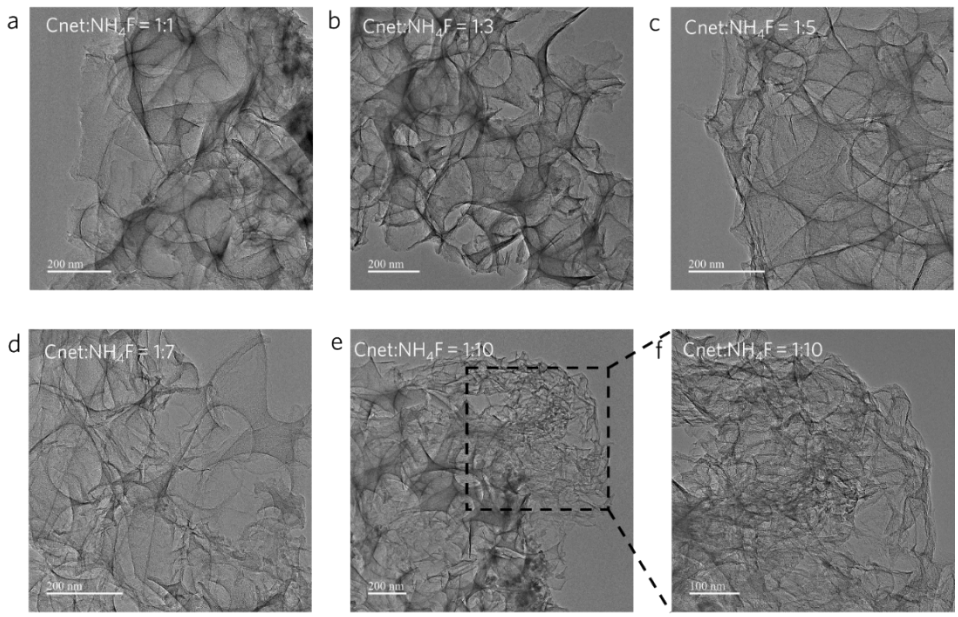

Figure S3. TEM images of F-Cnet prepared at different Cnet: NH_4F mass ratios (1:1, 1:3, 1:5, 1:7, 1:10), showing morphology evolution.

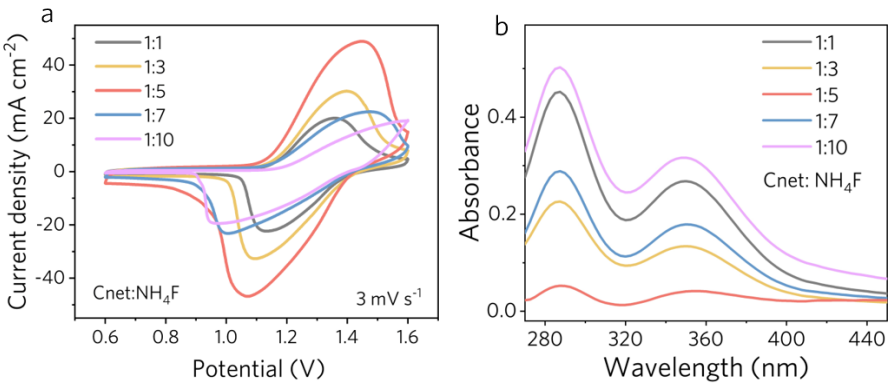

Figure S4. (a) CV curves of I_2@F-Cnet at 3 mV s^{-1} of F-Cnet prepared at different Cnet: NH_4F mass ratios (1:1, 1:3, 1:5, 1:7, 1:10). (b) UV-vis absorption spectra of the 2M $ZnSO_4$ electrolytes after static immersion of I_2@Cnet: NH_4F cathodes with different fluorination levels (mass ratios of 1:1, 1:3, 1:5, 1:7, and 1:10).

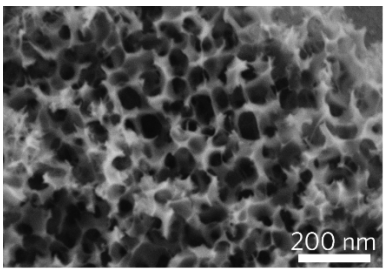

Figure S5. SEM image of Cnet.

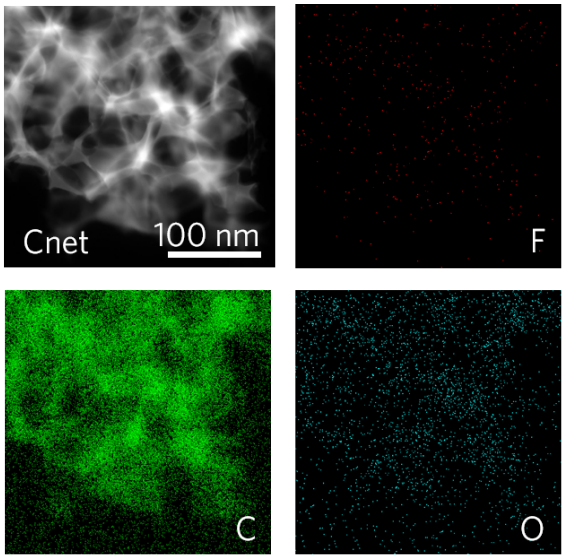

Figure S6. Elemental mapping of pristine Cnet.

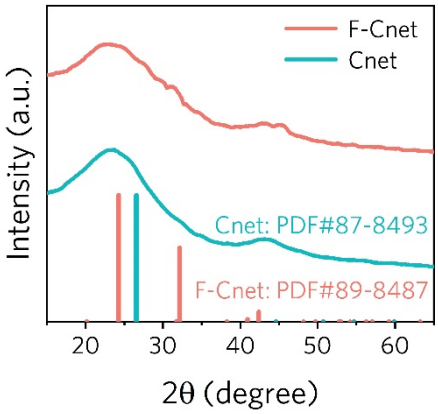

Figure S7. XRD patterns of Cnet and F-Cnet.

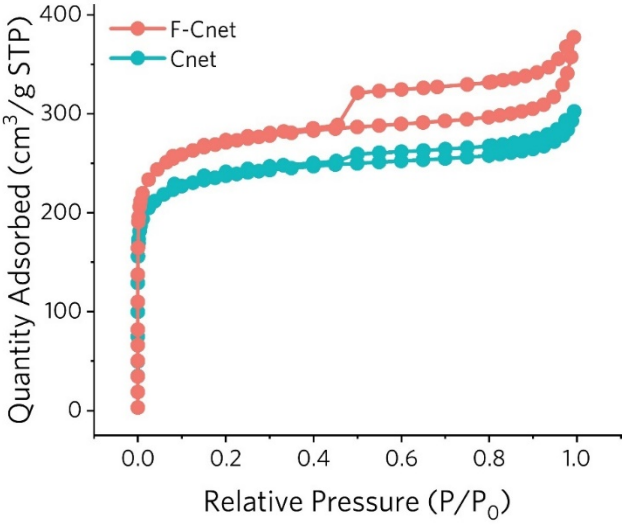

Figure S8. N_2 adsorption-desorption isotherms of Cnet and F-Cnet.

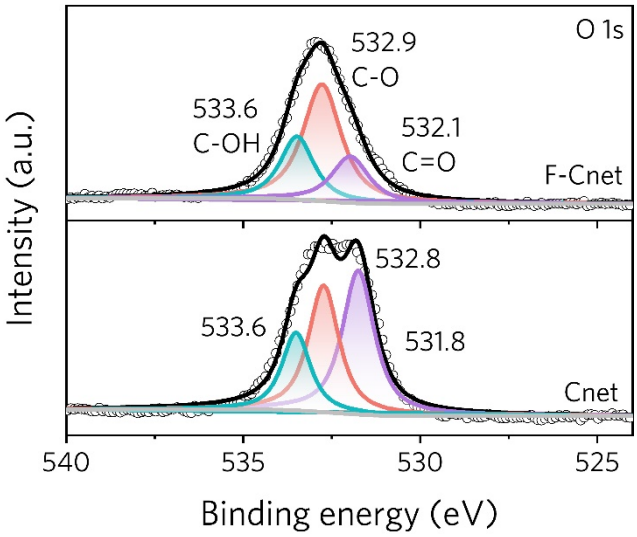

Figure S9. High-resolution O 1s XPS spectra of Cnet and F-Cnet.

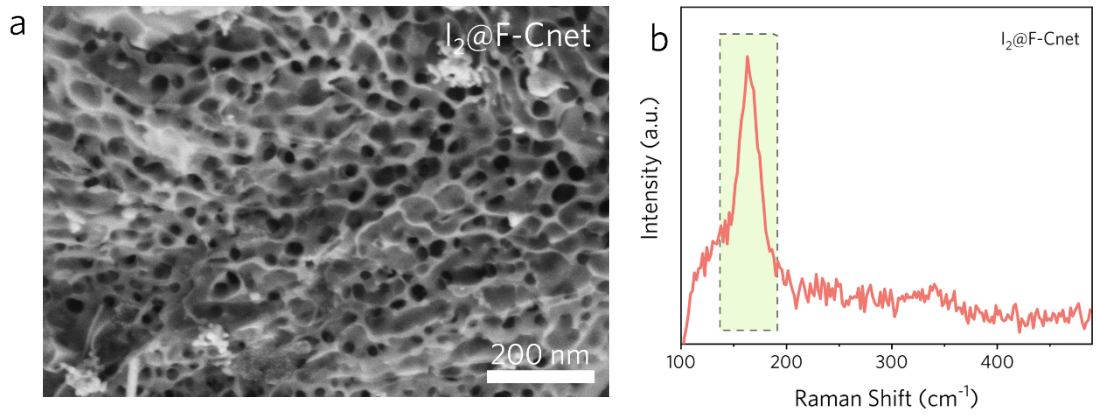

Figure S10. (a) SEM images of I_2@F-Cnet electrode. (b) Raman of I_2@F-Cnet electrode.

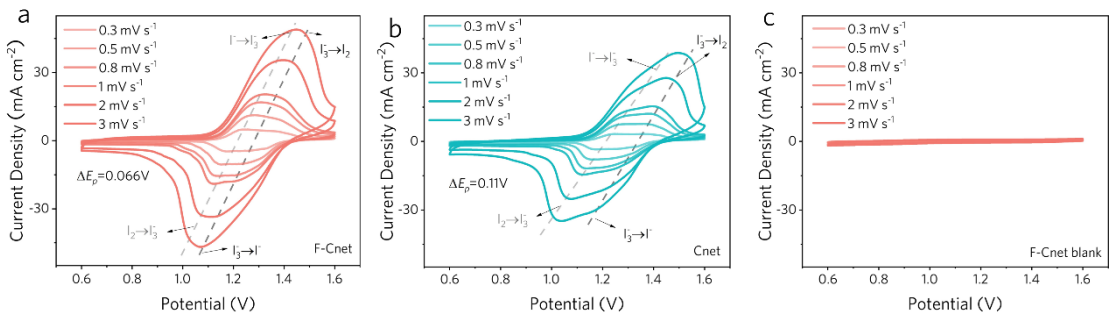

Figure S11. (a, b) CV curves of I_2@Cnet and I_2@F-Cnet electrodes at scan rates of 0.3-3 mV s^{-1}. (c) CV curve of blank F-Cnet electrode without iodine.

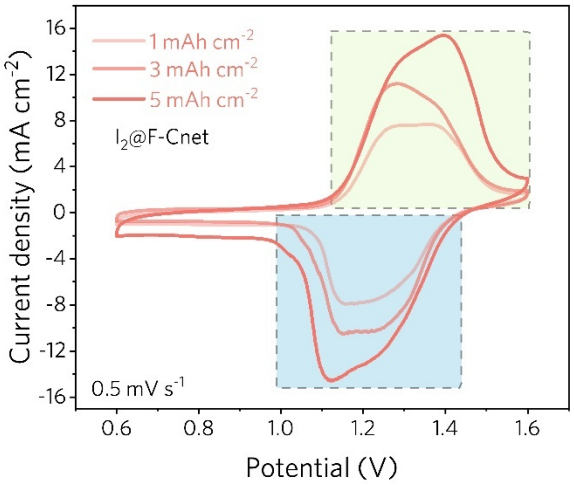

Figure S12. CV curves of I_2@F-Cnet at 0.5 mV s^{-1} of F-Cnet prepared at different iodine loading (1, 3, and 5 mAh cm^{-2}).

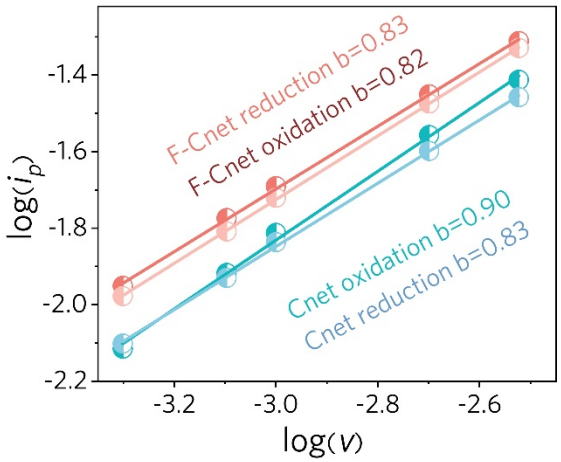

Figure S13. Fitting of log i_p versus log v for anodic and cathodic peaks of I_2@Cnet and I_2@F-Cnet electrodes.

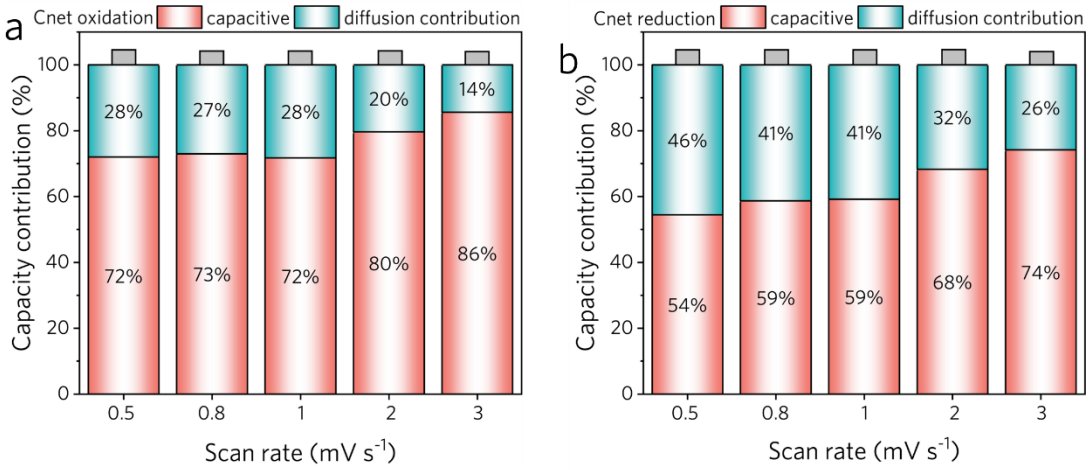

Figure S14. Capacitive and diffusion contributions of I_2@Cnet with oxidation (a) and reduction (b) at different scan rates.

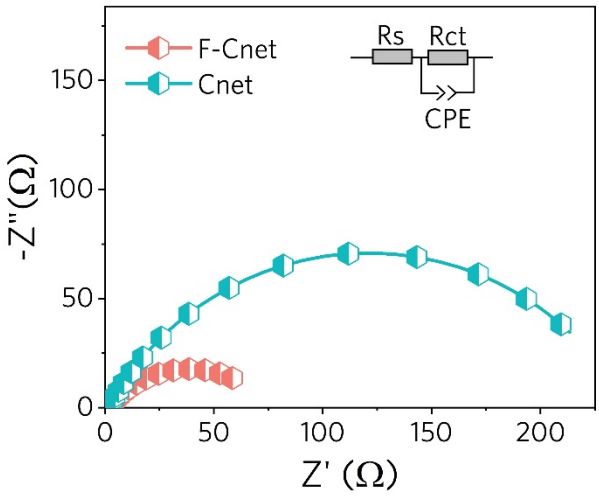

Figure S15. EIS spectra of I_2@F-Cnet and I_2@Cnet cathodes at the open-circuit voltage.

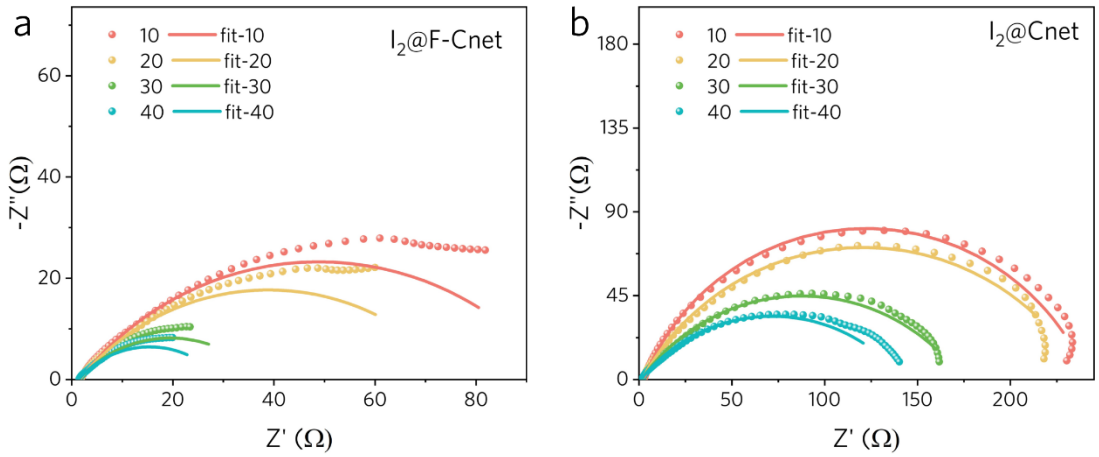

Figure S16. Temperature dependent electrochemical EIS of I_2@F-Cnet (a) and I_2@Cnet (b) cathodes at the onset potential.

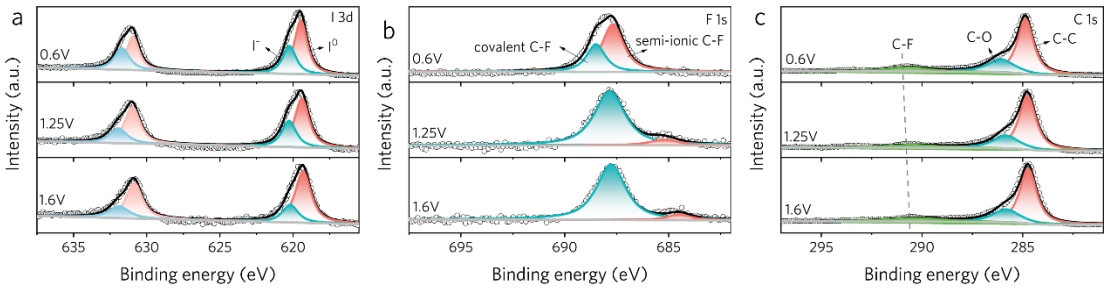

Figure S17. High resolution I 3d (a), F 1s (b), and C 1s (c) XPS spectra of the I_2@F-Cnet cathodes at different SOCs.

Note: As the SOC increases, the peaks associated with elemental iodine (I_0) at 619.4 and 630.9 eV slightly intensify, while the peaks corresponding to iodide (I^-) at 620.2 and 632.0 eV decrease (Figure S17a). This indicates that during the charge/discharge cycles, iodine on the electrode surface gradually transitions to higher oxidation states, such as I_2 and I_3^-, which supports efficient iodine conversion. This transformation enhances the electrochemical activity of the iodine species and facilitates faster redox kinetics. The F 1s spectrum (Figure S17b) reveals dynamic changes in the bonding environment at different SOCs. At 0.6 V, the semi-ionic C-F bond peak is observed at 687.6 eV. As the SOC increases, this peak diminishes and shifts to lower binding energies: 685.3 eV at 1.25 V and 684.6 eV at 1.6 V. Simultaneously, the covalent C-F bond peak at 688.4 eV becomes more prominent at higher potentials. This shift in the F-Cnet surface from semi-ionic to covalent C-F bonds suggests an enhancement of the material's structural stability and an improved interaction between the electrode surface and iodine species in the electrolyte. The C 1s spectrum (Figure S17c) shows shifts in the C-F and C-O peaks, reflecting the dynamic optimization of the carbon backbone's electronic structure during cycling. The C-C peak remains relatively stable, indicating that, aside from the subtle changes in functional groups associated with fluorine and oxygen, the carbon backbone maintains its mechanical integrity throughout the charge/discharge processes. This suggests that F-Cnet retains a robust structure even under electrochemical stress.

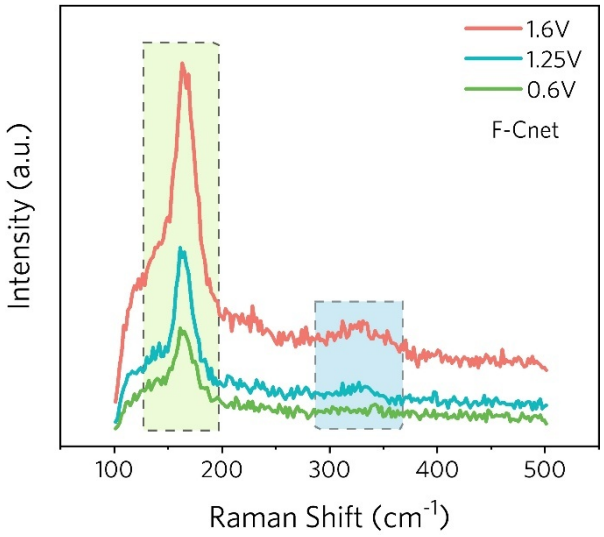

Figure S18. The Raman spectra at different SOCs on F-Cnet electrode.

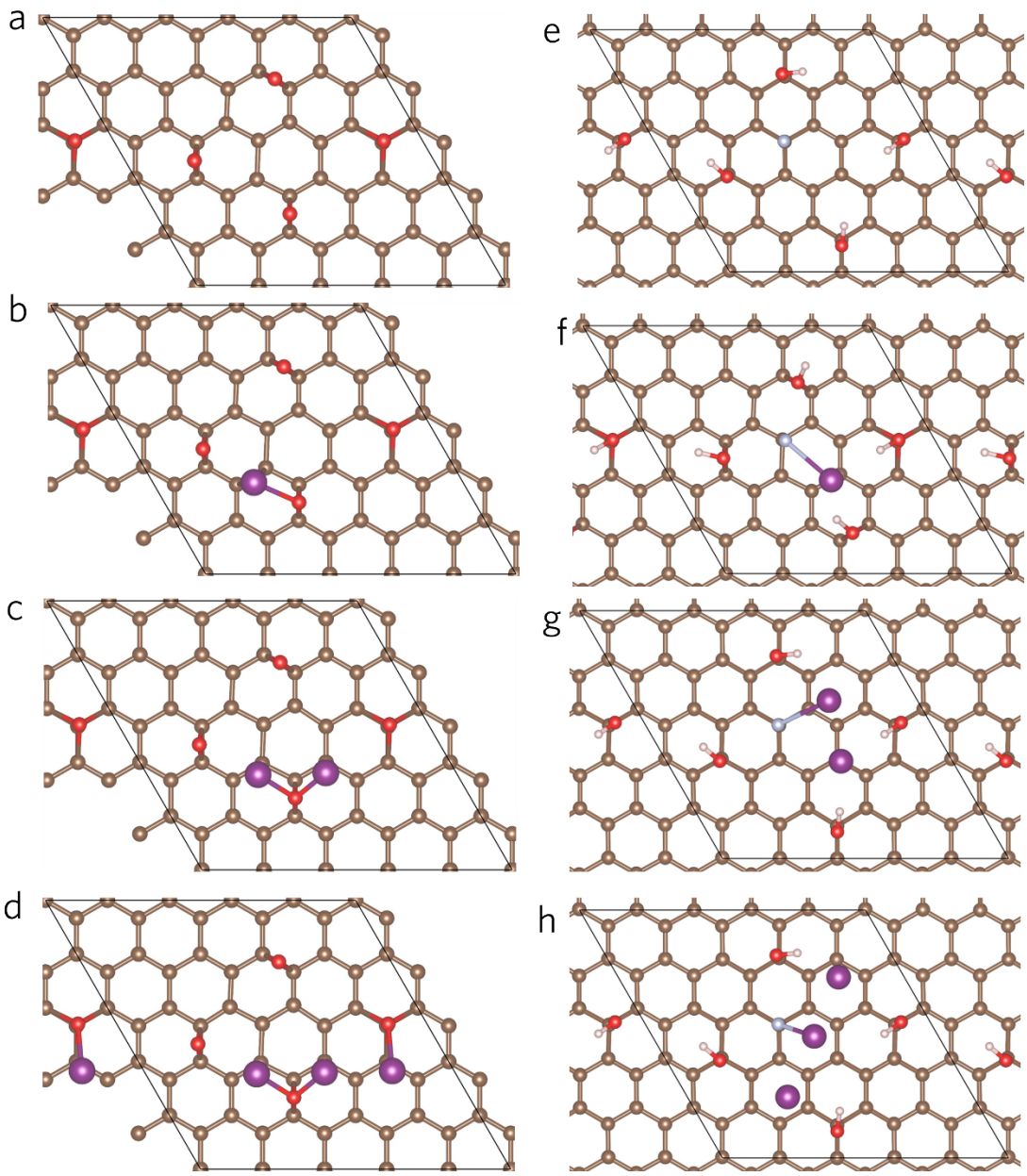

Figure S19. The optimized configuration for Cnet, Cnet-I*, Cnet-I_2*, Cnet-I_3* (a-d) and F-Cnet, F-Cnet-I*, F-Cnet-I_2*, F-Cnet-I_3* (e-h) from top-view. Red, pink, purple, brown and grey spheres represent O, H, I, C and F atoms, respectively.

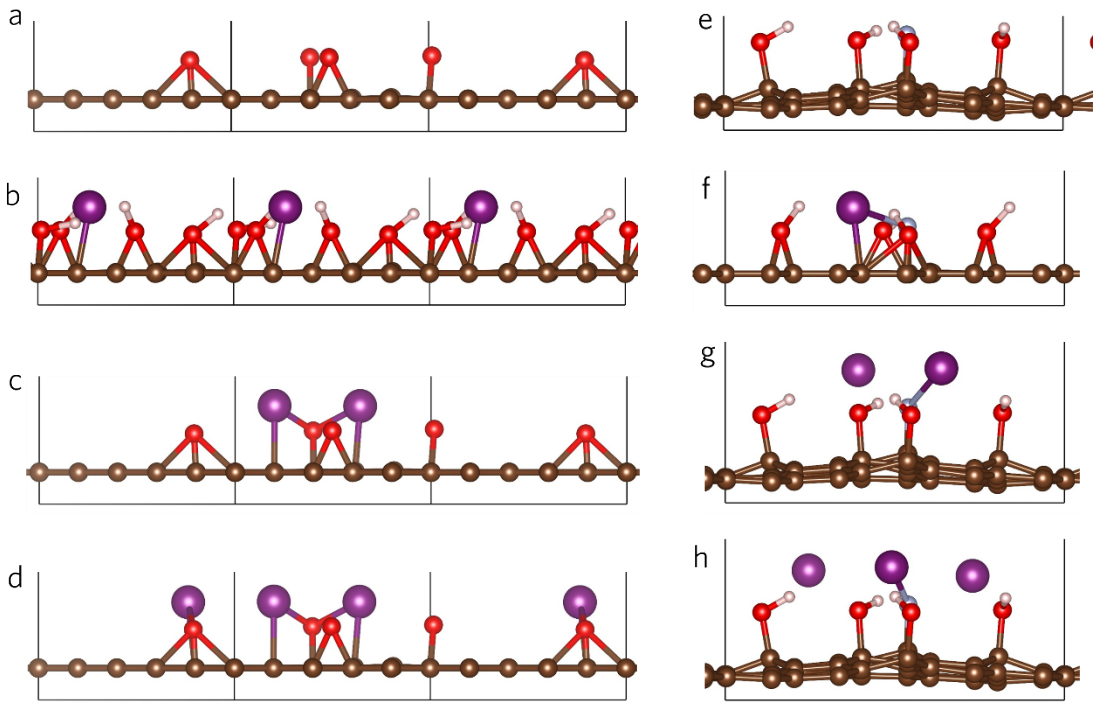

Figure S20. The optimized configuration for Cnet, Cnet-I*, Cnet-I_2*, Cnet-I_3* (a-d) and F-Cnet, F-Cnet-I*, F-Cnet-I_2*, F-Cnet-I_3* (e-h) from side-view. Red, pink, purple, brown and grey spheres represent O, H, I, C and F atoms, respectively.

Note: In our DFT calculations, the F-Cnet surface is modeled as a carbon framework containing locally fluorinated C–F/CF_xO_y sites, while the Cnet model shares the same carbon backbone but without fluorine. To experimentally substantiate the fluorination level relevant to this local model, we quantified the F content of Cnet and F-Cnet by oxygen-bomb combustion followed by ion chromatography (CIC, Figure 2i). The main peak at 3.2 min is assigned to F^-, from which we obtain 11.98 wt% F for F-Cnet and only 0.17 wt% F for Cnet, consistent with a partially fluorinated carbon framework bearing dispersed F functionalities rather than an undoped carbon host. This experimentally verified fluorine content supports the density of F sites used in our DFT slab and underpins the calculated enhancement in iodine adsorption on F-Cnet. The iodine-containing species in the DFT study are treated as adsorbed intermediates denoted I*, I_2*, and I_3* on Cnet and F-Cnet. Within plane-wave DFT and periodic boundary conditions, iodine atoms or polyiodide fragments are initially placed near candidate adsorption sites and then fully relaxed; the equilibrium bonding pattern (molecular, partially dissociated, or surface-bridged) and the corresponding adsorption energies emerge self-consistently from the electronic structure optimization, without manually imposing I-I bonds. In this work, the DFT results are therefore used in a comparative manner to elucidate how fluorine doping strengthens iodine binding and modulates the electronic structure.

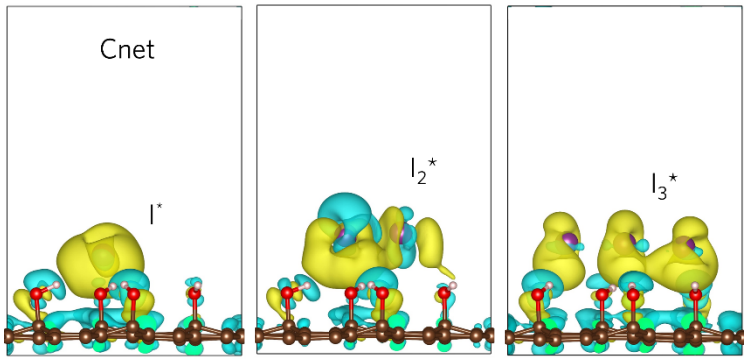

Figure S21. The charge density difference maps for Cnet-I*, Cnet-I_2* and Cnet-I_3* from side-view, where the yellow and cyan regions indicate the charge accumulation and depletion with the charge density isosurface was 0.0015 e $Å^{-3}$, respectively. Red, pink, purple, brown and grey spheres represent O, H, I, C and F atoms, respectively.

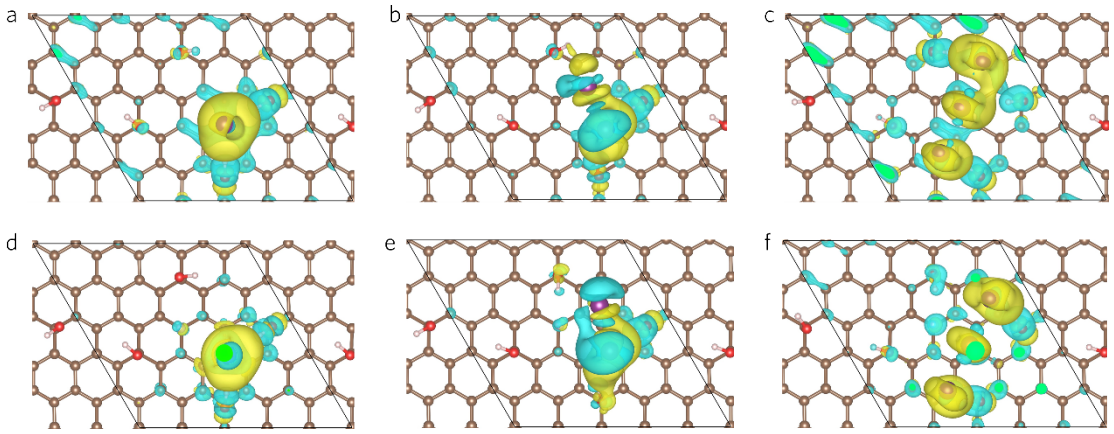

Figure S22. The charge density difference maps for Cnet-I*, Cnet-I_2*, Cnet-I_3* (a-c) and F-Cnet-I*, F-Cnet-I_2*, F-Cnet-I_3* (d-e) from top-view, where the yellow and cyan regions indicate the charge accumulation and depletion with the charge density isosurface was 0.0015 e $Å^{-3}$, respectively. Red, pink, purple, brown and grey spheres represent O, H, I, C and F atoms, respectively.

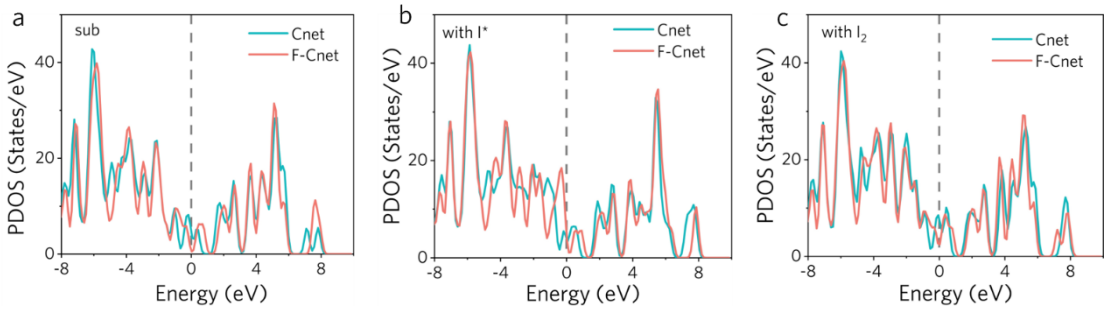

Figure S23. The PDOS for pure (a), I* (b), and I_2* (c) on F-Cnet and Cnet, with the line representing the Feimi level.

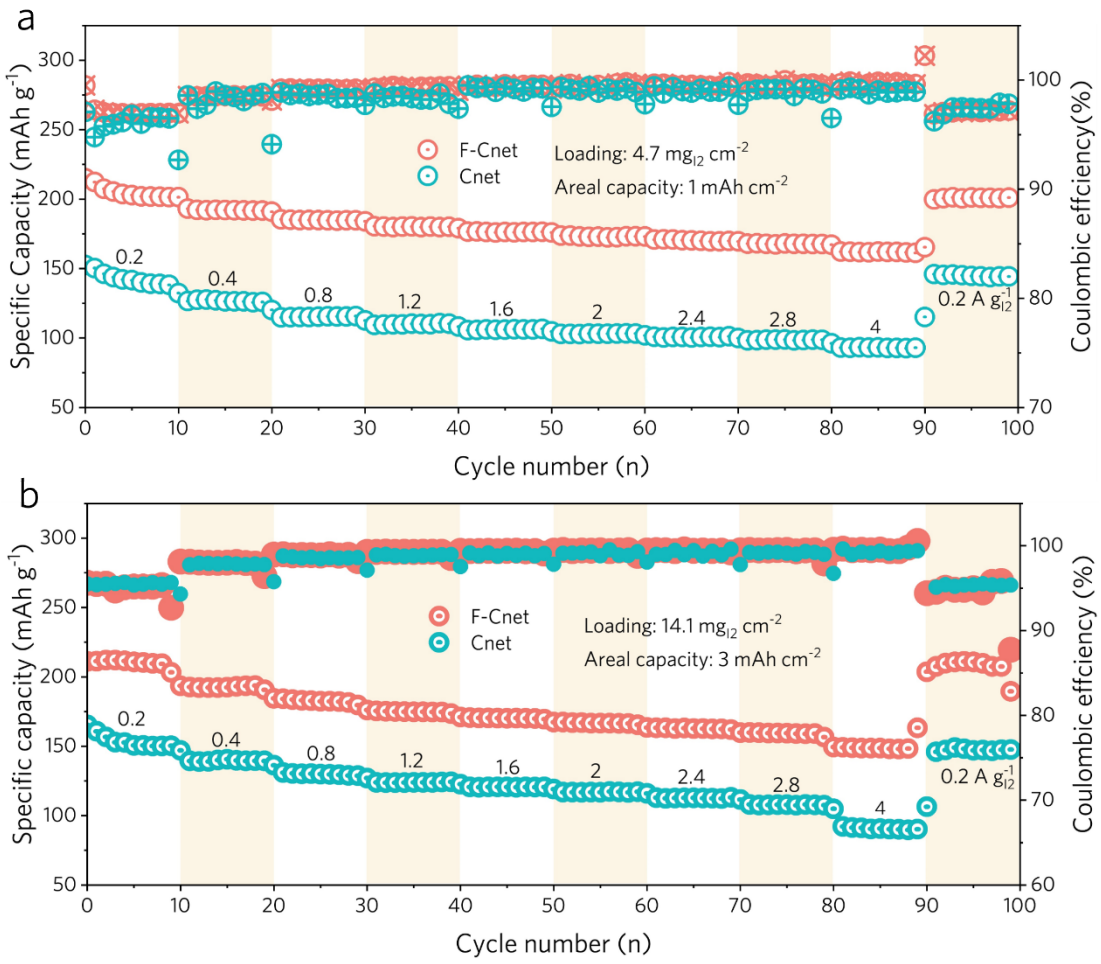

Figure S24. Rate performance of I_2@F-Cnet and I_2@Cnet electrodes at different current densities ranging from 0.2 to 4.0 A g_{I2}^{-1} with 1 (a) and 3 (b) mAh cm^{-2}.

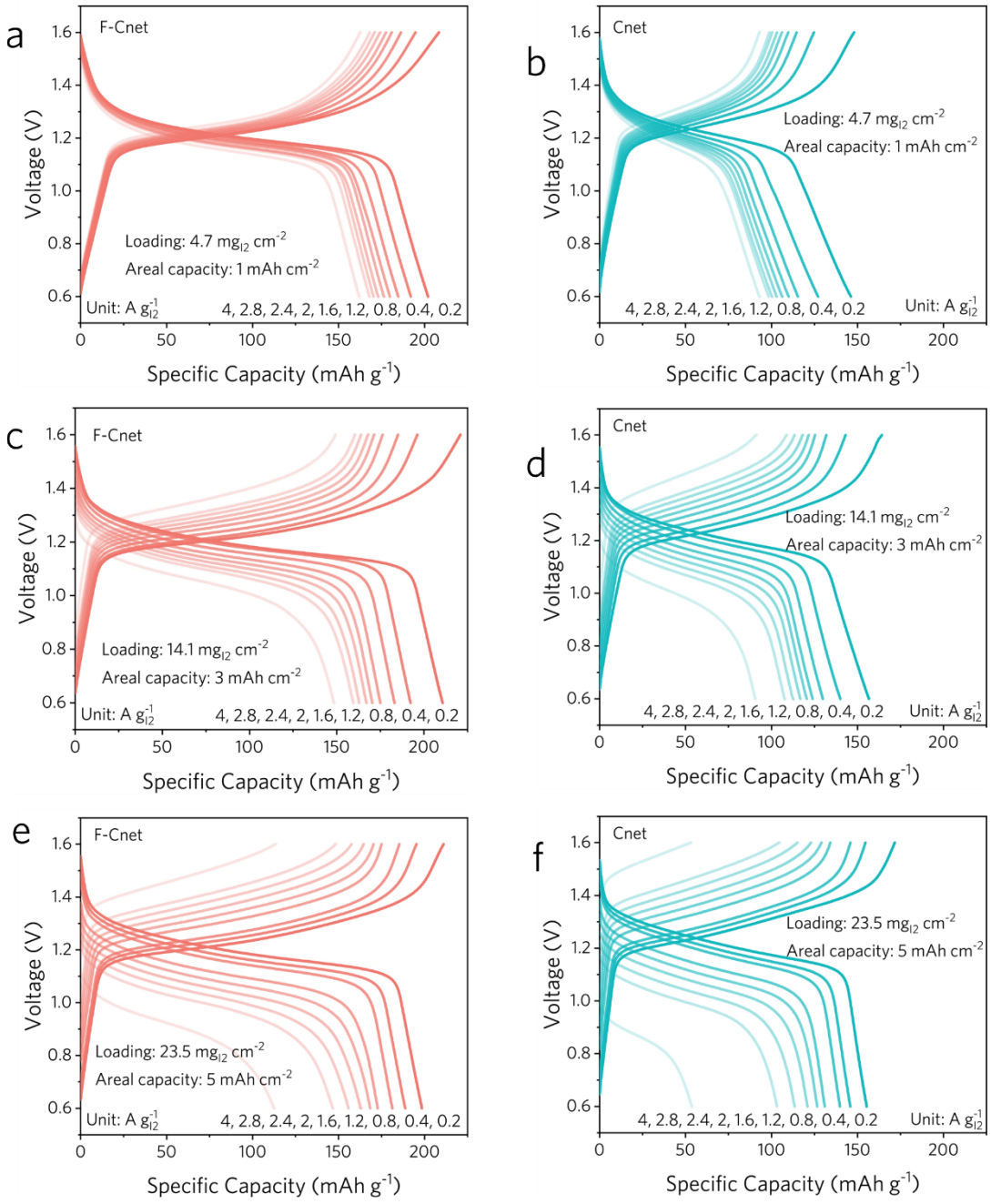

Figure S25. GCD curves at different current densities ranging from 0.2 to 4.0 A g_{I2}^{-1} of I_2@F-Cnet and I_2@Cnet electrodes with various areal capacities 1 (a, b), 3 (c, d) and 5 (e, f) mAh cm^{-2}.

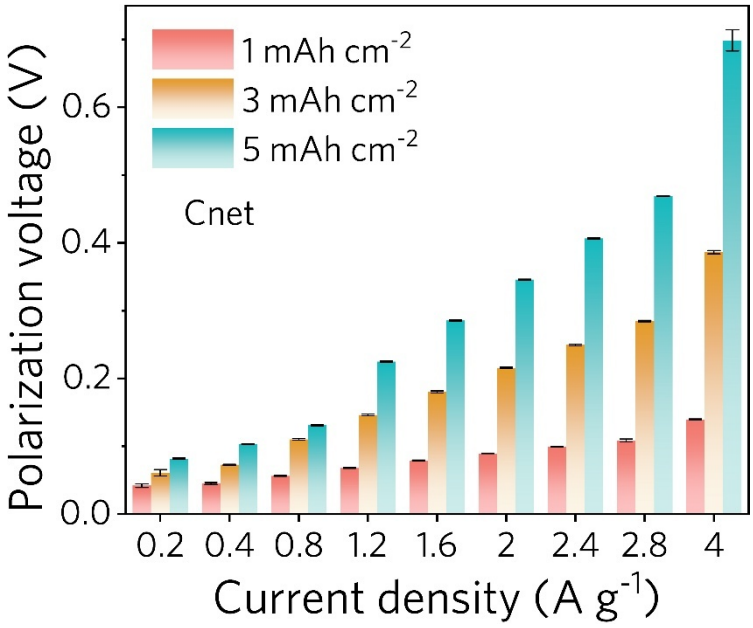

Figure S26. Comparison of polarization voltages at different current densities for Cnet with 1, 3, and 5 mAh cm^{-2} areal capacities.

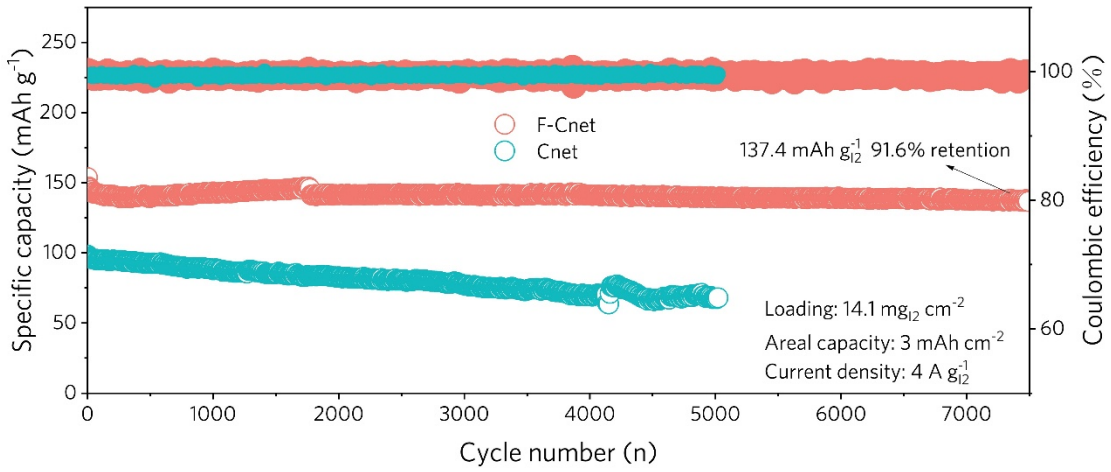

Figure S27. Cycling reversibility of batteries with different cathodes at 4 A g_{I2}^{-1} with 3 mAh cm^{-2}.

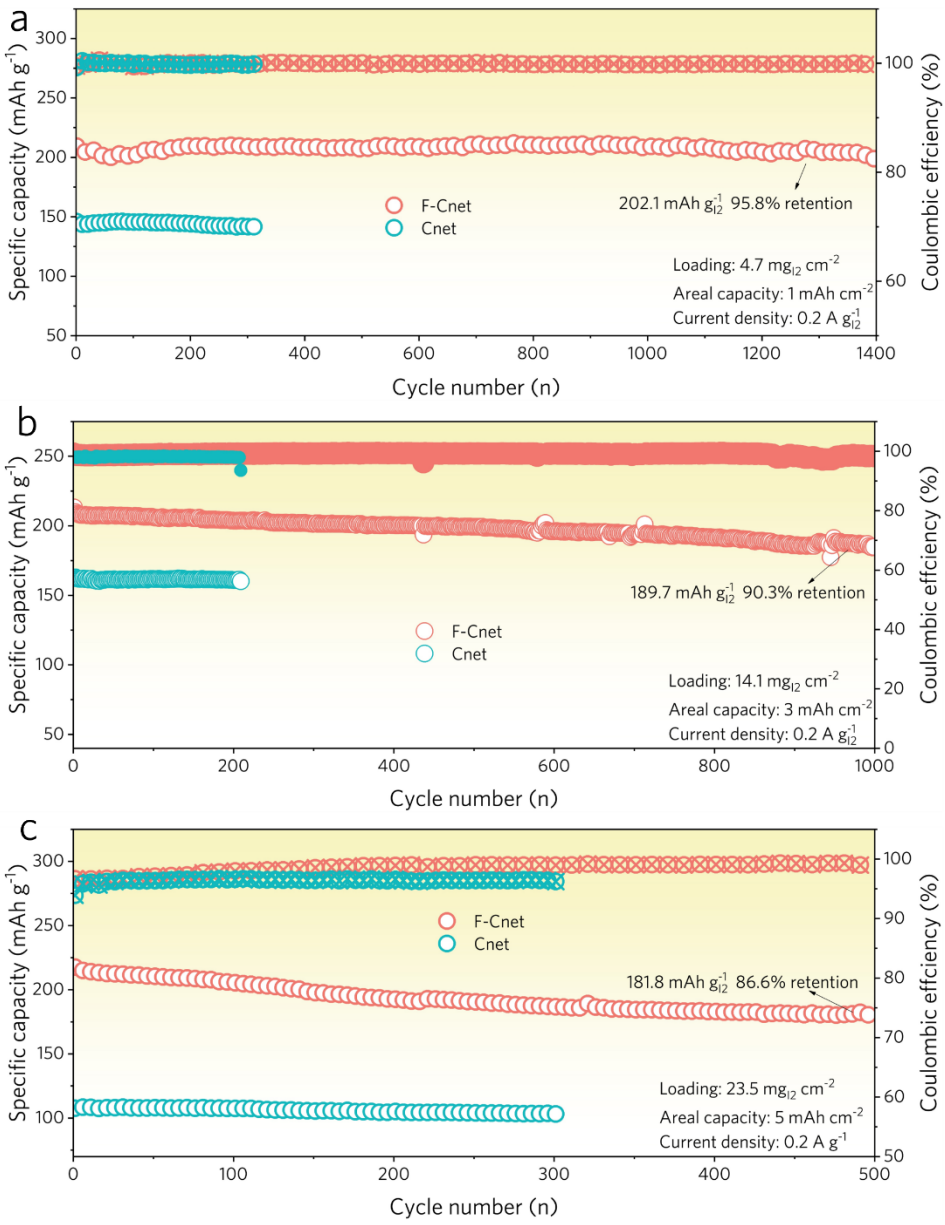

Figure S28. Cycling reversibility of batteries with different cathodes at 0.2 A g_{I2}^{-1} with 1, 3, and 5 mAh cm^{-2} areal capacities.

Note: At 1 mAh cm^{-2} (Figure S27a), F-Cnet demonstrates excellent cycle stability with 95.8% retention of its initial capacity after 1,400 cycles, retaining a specific capacity of 202.1 mAh g_{I2}^{-1}. In contrast, Cnet only retains a capacity of 148.6 mAh g_{I2}^{-1} after 350 cycles. At 3 mAh cm^{-2} (Figure S27b), F-Cnet shows 90.3% capacity retention, maintaining 189.7 mAh g_{I2}^{-1} after 1,000 cycles, while Cnet holds just retains a capacity of 157.8 mAh g_{I2}^{-1} after 200 cycles. At 5 mAh cm^{-2} (Figure S27c), F-Cnet retains 86.6% of its initial capacity, maintaining 181.8 mAh g_{I2}^{-1}, whereas Cnet exhibits only concludes at 105.2 mAh g_{I2}^{-1} after 300 cycles.

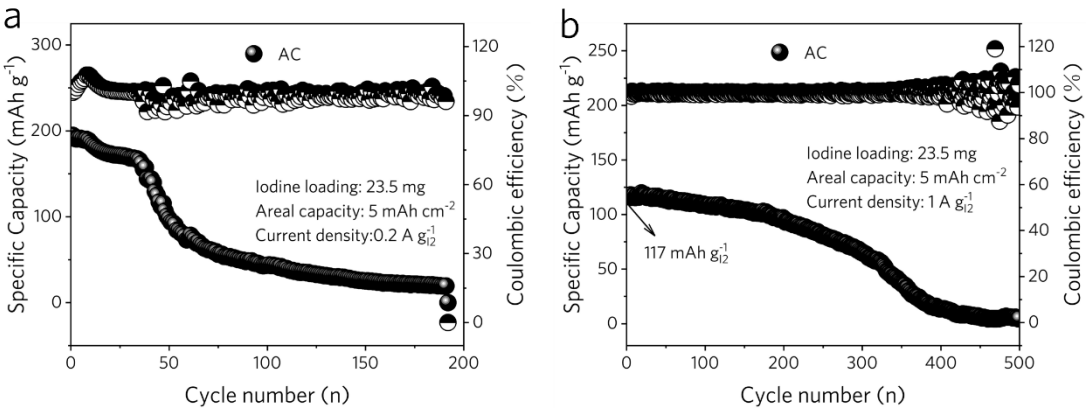

Figure S29. Cycling performance of batteries with I_2@AC cathode at 0.2 and 1 A g_{I2}^{-1} with 5 mAh cm^{-2}, 23.5 mg cm^{-2}.

Note: At a current density of 23.5 mA cm^{-2}, the initial specific capacity of the I_2@AC electrode is only 117 mAh g_{I2}^{-1}, with a 50% capacity loss (about 58.5 mAh g_{I2}^{-1}) after 250 cycles, and complete failure (capacity approaching 0) after 380 cycles. At a lower current density of 5 mA cm^{-2}, the initial capacity reaches 202 mAh g_{I2}^{-1}, but it decays to 101 mAh g_{I2}^{-1} after just 50 cycles and fails completely after 120 cycles. These results clearly indicate that commercial AC suffers from significant stability and durability issues at high areal capacities.

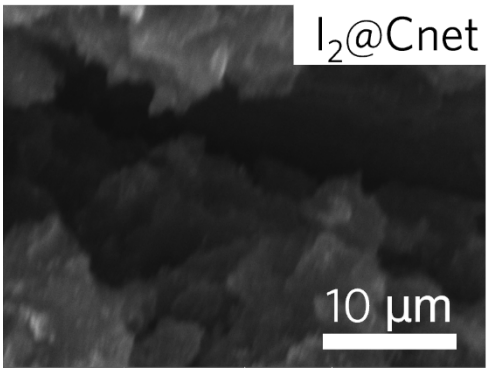

Figure S30. SEM image of I_2@Cnet electrodes after 500 cycles.

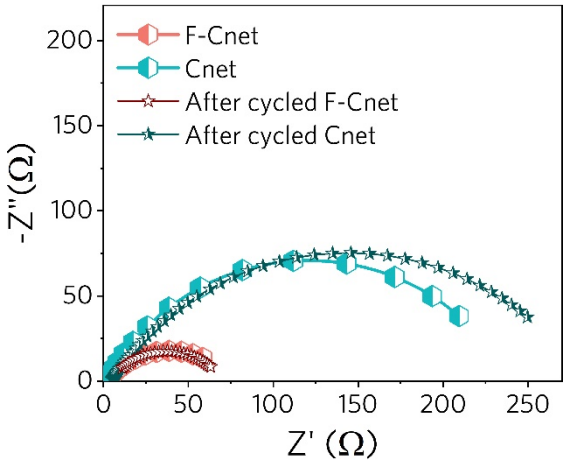

Figure S31. EIS spectra of I_2@F-Cnet and I_2@Cnet cathodes before and after 500 cycles at a current density of 4 A g^{-1}.

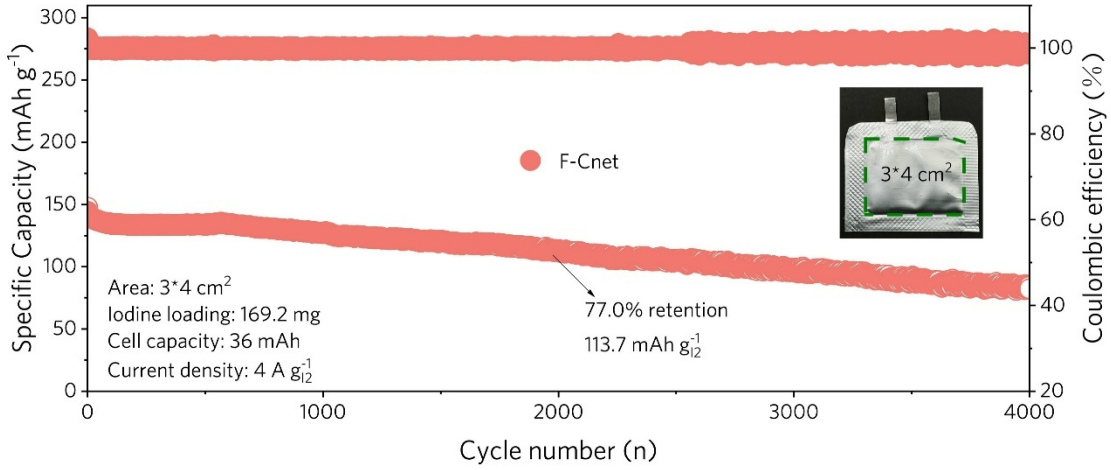

Figure S32. Cycling performance of the pouch cell at 4 A g_{I2}^{-1}.

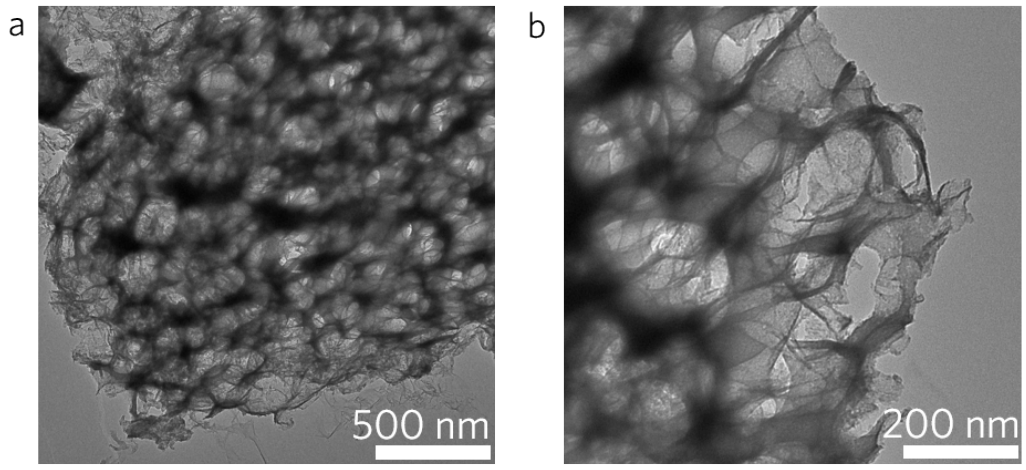

Figure S33. TEM images of F-Cnet after LDES.

Table S1. Comparison of various performance parameters with reported host materials for AZIBs.

Parameters	Areal capacity (mAh cm^{-2})	Cycle specific capacity (mAh g_{I2}^{-1})	Cycle number (n) (Capacity retention)	Ref.
B-Fe-N/I_2	1.0	180 (5C) 168 (10C)	5,000 (87%) 10,000 (85%)	1[11]
PC@Fe_2N-4/I_2	0.3	148.5 (2C) 153 (10C)	200 (77%) 20,000 (77%)	2[12]
I_2@NPCNFs-800	0.3	118.5 (2C)	6,000 (94%)	3[13]
I_2@PAF-1	0.4	101 (10C)	20,000 (86%)	4[14]
I_2/OSTC	0.7	157 (1 A g^{-1})	10,000 (85%)	5[15]
I_2@C-50	1.7	89 (5 A g^{-1})	10,000 (66%)	6[16]
PNC-1000-I_2	0.7	190 (0.2 A g^{-1}) 155 (4 A g^{-1})	3,000 (84%) 10,000 (88%)	7[17]
I_2@F-Cnet	5.0	194.5 (0.0355 A g^{-1}) 164.4 (4 A g^{-1})	250 (89%) 14,000 (98%)	This work

Reference

1. Y. Shang and D. Kundu, *Joule*, 2023, **7**, 244-250.
2. H. Kim, S. K. Oh, J. Lee, S. W. Doo, Y. Kim and K. T. Lee, *Electrochim. Acta*, 2021, **370**, 137743.
3. Z. Li, W. Cao, T. Hu, Y. Hu, R. Zhang, H. Cui, F. Mo, C. Liu, C. Zhi and G. Liang, *Angew. Chem. Int. Ed.*, 2024, **63**, e202317652.
4. W. Cao, T. Hu, Y. Zhao, Z. Li, Y. Hu, C. Li, Y. Sun, F. Ding and G. Liang, *ACS Energy Lett.*, 2025, **10**, 320-329.
5. H. L. Pan, Y. Y. Shao, P. F. Yan, Y. W. Cheng, K. S. Han, Z. M. Nie, C. M. Wang, J. H. Yang, X. L. Li, P. Bhattacharya, K. T. Mueller and J. Liu, *Nat Energy*, 2016, **1**.
6. G. Kresse and J. Furthmüller, *Physical Review B*, 1996, **54**, 11169-11186.
7. J. P. Perdew, K. Burke and M. Ernzerhof, *Physical Review Letters*, 1996, **77**, 3865-3868.
8. A. Togo and I. Tanaka, *Scripta Materialia*, 2015, **108**, 1-5.
9. X. Gonze, J. C. Charlier, D. C. Allan and M. P. Teter, *Physical Review B*, 1994, **50**, 13035-13038.
10. Q. Y. Zhang and X. Y. Huang, *Progress in Materials Science*, 2010, **55**, 353-427.
11. M. Liu, Q. Chen, X. Cao, D. Tan, J. Ma and J. Zhang, *J. Am. Chem. Soc.*, 2022, **144**, 21683-21691.
12. Q. Chen, S. Chen, J. Ma, S. Ding and J. Zhang, *Nano Energy*, 2023, **117**, 108897.
13. Y. He, M. Liu, S. Chen and J. Zhang, *Sci. China Chem.*, 2022, **65**, 391-398.
14. J. Hu, Z. Zhang, T. Deng, F. C. Cui, X. Shi, Y. Tian and G. Zhu, *Adv. Mater.*, 2024, **36**, 2401091.
15. M. Chen, W. Zhu, H. Guo, Z. Tian, L. Zhang, J. Wang, T. Liu, F. Lai and J. Huang, *Energy Storage Mater.*, 2023, **59**, 102760.
16. W. Li, K. Wang and K. Jiang, *J. Mater. Chem. A*, 2020, **8**, 3785-3794.
17. T. Liu, H. Wang, C. Lei, Y. Mao, H. Wang, X. He and X. Liang, *Energy Storage Mater.*, 2022, **53**, 544-551.